GEOCHEMISTRY

Photoferrotrophy, deposition of banded iron formations, and methane production in Archean oceans

Katharine J. Thompson[1], Paul A. Kenward[1], Kohen W. Bauer[1], Tyler Warchola[2], Tina Gauger[3], Raul Martinez[4], Rachel L. Simister[1], Céline C. Michiels[1], Marc Llirós[5], Christopher T. Reinhard[6], Andreas Kappler[3], Kurt O. Konhauser[2], Sean A. Crowe[1]*

Banded iron formation (BIF) deposition was the likely result of oxidation of ferrous iron in seawater by either oxygenic photosynthesis or iron-dependent anoxygenic photosynthesis—photoferrotrophy. BIF deposition, however, remains enigmatic because the photosynthetic biomass produced during iron oxidation is conspicuously absent from BIFs. We have addressed this enigma through experiments with photosynthetic bacteria and modeling of biogeochemical cycling in the Archean oceans. Our experiments reveal that, in the presence of silica, photoferrotroph cell surfaces repel iron (oxyhydr)oxides. In silica-rich Precambrian seawater, this repulsion would separate biomass from ferric iron and would lead to large-scale deposition of BIFs lean in organic matter. Excess biomass not deposited with BIF would have deposited in coastal sediments, formed organic-rich shales, and fueled microbial methanogenesis. As a result, the deposition of BIFs by photoferrotrophs would have contributed fluxes of methane to the atmosphere and thus helped to stabilize Earth's climate under a dim early Sun.

INTRODUCTION

Banded iron formations (BIFs) host the world's largest iron ore deposits, and they formed predominantly through the deposition of ferric iron [Fe(III)] from ferruginous oceans during the Archean Eon (*1*, *2*). Most models for BIF deposition invoke photosynthesis in the oxidation of ferrous iron from seawater to induce its subsequent precipitation and deposition as mixed valence iron (oxyhydr) oxides and carbonate phases (*3*–*6*) [see (*7*) and (*8*) for alternative models]. BIFs thus likely record the activity of Earth's early photosynthetic biosphere (*3*). Two modes of photosynthesis have been implicated in Fe(II) oxidation—canonical oxygenic photosynthesis by the ancestors of modern cyanobacteria (*3*) and iron-dependent anoxygenic photosynthesis (*4*, *5*), referred to as photoferrotrophy. Photoferrotrophic bacteria grow using light and Fe(II) to fix CO_2 into biomass and produce Fe(III) as a metabolic by-product (*5*, *6*, *9*)–they can do so in the complete absence of oxygen (*9*). Current literature suggests that this anoxygenic photosynthesis is likely the evolutionary predecessor of oxygenic photosynthesis (*10*–*12*) and that Fe(II) oxidation could thus have been driven by photoferrotrophy before the emergence and proliferation of oxygenic photosynthesis (*13*, *14*). Models of nutrient cycling in the Archean ocean implicate photoferrotrophs as key primary producers (*13*, *15*) before the rise of atmospheric oxygen 2.4 to 2.3 billion years (Ga) ago during the Great Oxidation Event (GOE) (*16*–*18*). High methane concentrations in the Archean atmosphere have also been qualitatively attributed to C and Fe cycling associated with BIF deposition (*19*). Such an "upside-down" biosphere (*19*), in which the reduced products of photosynthesis end up in the atmosphere as methane and the oxidized products are buried as Fe(III) in BIF, can, as we show here, be quantitatively and mechanistically linked to the activity of photoferrotrophs in ferruginous Archean oceans.

Observations and models of extant photoferrotrophs demonstrate their capacity to both oxidize Fe(II) at rates sufficient to form even the largest BIFs and support appreciable rates of primary production (*5*, *13*, *20*, *21*). Laboratory experiments to date, paradoxically, reveal a tight physical association between photosynthetic ferric iron metabolic by-products [e.g., Fe(III) (oxyhydr)oxides] and cellular biomass that leads to their co-sedimentation (*5*, *20*, *22*). In the oceans, the deposition of Fe(III), along with this photosynthetic biomass, would fuel sedimentary respiration that couples oxidation of organic carbon to microbial Fe(III) mineral reduction and converts Fe(III) to dissolved Fe(II) and secondary minerals such as siderite and magnetite (*22*). This sedimentary respiration thus closes the iron redox cycle and precludes the preservation of ferric iron in BIF. Current observations and models therefore cannot explain BIF deposition through photoferrotrophy in light of this co-sedimentation of biomass with Fe(III) and ensuing diagenetic reactions (*22*, *23*). By contrast, a lack of Fe(III) reduction would lead to the co-deposition of ferric iron in BIF, with organic matter at relative concentrations close to the 4:1 stoichiometry of Fe(II) oxidation to C fixation in photoferrotrophy [e.g., ~2 weight % (wt %) C based on 37 wt % Fe(III) in Dales Gorge BIF (*24*)]. A compilation of organic matter concentrations and Fe redox states in BIFs, however, reveals that they have very low organic matter concentrations (mean of 0.27 wt %; Fig. 1 and table S5) (*24*, *25*) and contain appreciable Fe(III), with an average Fe redox state of 2.6 (fig. S1 and table S5) (*24*, *25*). If the iron minerals in BIFs were the product of photosynthesis, then the fate of the corresponding photosynthetic biomass remains entirely enigmatic. Furthermore, regardless of the mode of Fe(II) oxidation, current estimates for the magnitude of hydrothermal Fe(II) fluxes to the Archean ocean appear to be deficient of the mass fluxes needed to sustain BIF deposition (*26*) and may imply an important role for terrestrial weathering fluxes (*27*, *28*). We thus combined experiments

[1]Departments of Microbiology and Immunology and Earth, Ocean, and Atmospheric Sciences, University of British Columbia, Vancouver, British Columbia, Canada. [2]Department of Earth and Atmospheric Sciences, University of Alberta, Edmonton, Alberta T6G 2E3, Canada. [3]Center for Applied Geosciences, University of Tuebingen, 72076 Tuebingen, Germany. [4]Institut für Geo- und Umweltnaturwissenschaften, Albert-Ludwigs-Universität, Mineralogie-Geochemie, 79104 Freiburg, Germany. [5]Department of Genetics and Microbiology, BioSciences Faculty, Universitat Autònoma de Barcelona, Catalunya, Spain. [6]School of Earth and Atmospheric Sciences, Georgia Institute of Technology, Atlanta, GA, USA.
*Corresponding author. Email: sean.crowe@ubc.ca

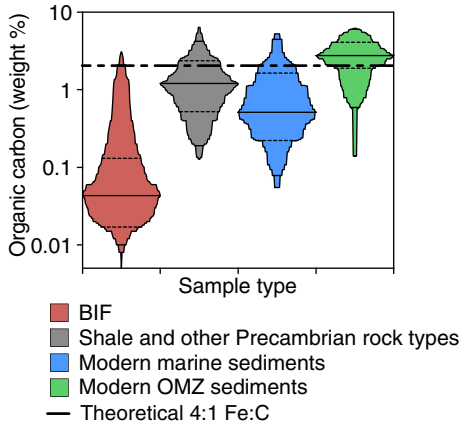

Fig. 1. The organic matter concentrations in BIFs, other Precambrian sedimentary rocks, typical modern marine sediments, and oxygen minimum zone (OMZ) sediments. The solid lines represent the group means, while the dotted lines delineate one SD above and below the mean. The black dashed line that spans the figure represents the theoretical organic carbon concentration that would be expected in BIFs deposited by photoferrotrophs (2.04 wt % C), assuming quantitative co-sedimentation of biomass with ferric Fe. References for this figure can be found in table S5.

using modern photosynthetic bacteria with revised theoretical estimates of Fe(II) fluxes to the Archean ocean and box modeling of coupled carbon and iron cycling to show that photosynthetic Fe(II) oxidation could have sustained large-scale, organic-poor BIF deposition in ocean upwelling systems over hundreds of millions of years.

RESULTS AND DISCUSSION

Separation of biomass and Fe(III)

To explore the fate of biomass and Fe(III) during photosynthetic Fe(II) oxidation, we conducted experiments using *Chlorobium phaeoferrooxidans* strain KB01–a photoferrotrophic bacterium that was isolated from the water column of ferruginous Kabuno Bay, a sub-basin of Lake Kivu in East Africa (*21*). We also conducted experiments with *Chlorobium ferrooxidans* strain KoFox, a sediment-dwelling photoferrotroph that tends to associate with Fe(III) (oxyhydr)oxides without becoming encrusted (*23*, *29*), as well as a model marine oxyphototrophic cyanobacterium of the genus *Synechococcus*. Strain KB01 is the only known photoferrotroph from a pelagic environment (*21*), and pelagic photoferrotrophs, including those that would have populated Precambrian ferruginous oceans, face a special challenge—they must maintain their position within sunlit waters despite the precipitation of heavy Fe(III) oxyhydroxide metabolic by-products that have a tendency to adhere to cell surfaces and cause their rapid sedimentation. Most bacteria have negatively charged cell surfaces at neutral pH (*30*), while Fe(III) (oxyhydr)oxides typically have a positive surface charge at the same pH (*31*). This generally leads to a strong attraction between cell surfaces and Fe(III) (oxyhydr)oxides that often manifests as encrustation of bacterial cells and formation of Fe(III) oxyhydroxide cell aggregates (*6*, *32*).

To test the association between photoferrotrophs and their Fe(III) metabolic by-products, we grew strain KB01 until late exponential growth phase, gently inverted the cell-mineral suspension to resuspend sedimented Fe(III) (oxyhydr)oxides and cells, allowed the heavy Fe(III) (oxyhydr)oxides to resettle, and determined the percentage of cells that remained suspended (Fig. 2A). Experiments conducted in media with reduced phosphate concentrations (3 to 6 μM), approaching those of modern seawater but still somewhat higher than the submicromolar concentrations found in Precambrian seawater (*15*), show that 50% of strain KB01 cells are associated with Fe(III) (oxyhydr)oxides, leading to co-sedimentation of biomass and Fe(III) (Fig. 2A). While phosphate concentrations were very low in the seawater from which BIFs deposited (*15*, *33*), silica concentrations in Precambrian oceans were high (~1 mM) (*15*), and this would have altered the physical and chemical properties of Fe(III) precipitates formed in seawater (*33*). In experiments with 1 mM silica, the concentration implied for Precambrian seawater (*15*), strain KB01 cells did not associate to, or co-sediment with, their Fe(III) oxyhydroxide by-products (Fig. 2A). Instead, almost all of the cells remained suspended (94 ± 6%). Likewise, experiments conducted with strain KoFox demonstrated that cell-mineral association was diminished relative to the silica-free experiments, with 72 ± 7% of strain KoFox cells remaining suspended (Fig. 2A and fig. S5A). We also grew both strains KB01 and KoFox in their standard growth medium containing 4 mM phosphate and no silica, which led to little cell-mineral association for strain KB01 (Fig. 2A) and modest association for strain KoFox (fig. S5A). Detailed electron microscopy revealed that the surfaces of KB01 cells were entirely free from Fe(III) oxyhydroxide precipitates (Fig. 3), whereas strain KoFox tended to form multicellular aggregates that variably associated with the mineral precipitates (fig. S3A). Strain KB01, and to a somewhat lesser extent strain KoFox, thus avoids encrustation with Fe in low-P, high-Si waters, as well as in standard growth media with high phosphate, remaining suspended despite Fe(III) oxyhydroxide precipitation.

We also subjected *Synechococcus* cells to Fe-Si–rich growth conditions in a similar fashion (Fig. 2A and fig. S5A). *Synechococcus* associated to a greater extent with the Fe(III) oxyhydroxide products of Fe(II) oxidation than did the photoferrotrophs under these conditions. Such an association was expected, despite the presence of silica, given that oxygen effuses from *Synechococcus* cells, reacts rapidly with Fe(II), and causes precipitation of Fe(III) (oxyhydr)oxides on the cell surfaces—an association likely maintained due to binding with organic ligands, as observed in many previous environmental and laboratory studies (*32*, *34*, *35*). Photoferrotrophs adapted to pelagic lifestyles thus appear most capable of avoiding co-sedimentation with Fe(III) and remain buoyant with the potential for separation of biomass from Fe(III) at larger scales in the environment.

Mechanisms of cell-mineral separation

Surface charge often influences cell-mineral association, or lack thereof, and as solution P:Fe or Si:Fe ratios increased, the surface charge on the Fe(III) (oxyhydr)oxides formed became more negative (Fig. 2B) due to the incorporation of P or Si anions into the oxyhydroxide structure (*33*). Conversely, Fe(III) oxyhydroxide particles were positively charged under low P or Si conditions, which is consistent with observations of positively charged Fe(III) precipitates in many environments (*31*). Strain KB01 cells had strongly negative surface charges (fig. S4), whereas cells of strain KoFox had near neutral surface charges (fig. S4), similar to some microaerophillic Fe(II) oxidizers (*36*). This difference in surface charge between strains KB01 and KoFox reflects different cell surface chemistries (table S2), notably an abundance of anionic surface functional groups on strain KoFox with different acid-base behavior than strain KB01 (Supplementary Materials and fig. S3). Benthic microorganisms, such as strain KoFox, commonly produce surface

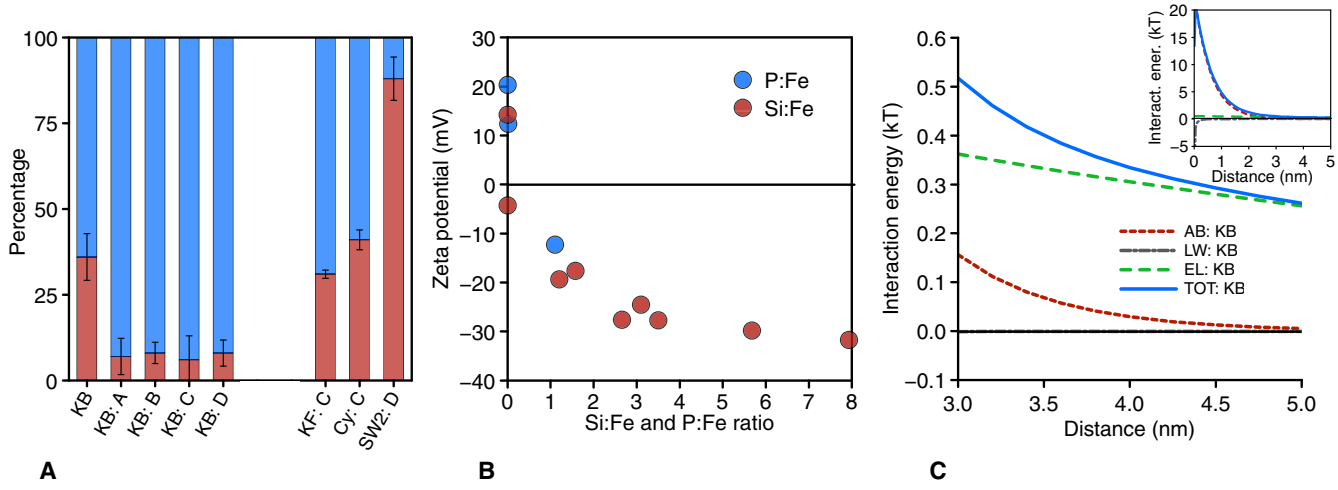

Fig. 2. Cell surface characteristics for strain KB01 and the relationship between ferric iron surface charge and medium anions. Fractions of planktonic (blue) versus sedimented (red) cells (**A**) for photoferrotrophic strain KB01 under varying geochemical conditions: 400 μM Fe(II) with low P (3 μM) [unmarked]; 400 μM Fe(II), low P (3 μM), with 0.6 mM Si [A]; 400 μM Fe(II), low P (3 μM), with 1.0 mM Si [B]; 400 μM Fe(II), low P (3 μM), with 1.5 mM Si [C]; and 10 mM Fe(II) with 4.4 mM P [D]. *C. ferrooxidans* and *Synechococcus* are also shown under the [C] conditions. *Rhodobacter* strain SW2 is shown under the [D] conditions. The zeta potential (**B**), in millivolts, of the ferric iron precipitates is depicted with an increasing ratio of Si or P to Fe, where the error bars are all within the data points. Last, for the extended DVLO modeling for strain KB01 (**C**), the main graph depicts the interaction energies of the three forces (AB, Lewis acid base; LW, Lifshitz–van der Waals; EL, electrostatic) and the total (TOT) for those forces from 3 to 5 nm, while the inset depicts the forces from 0 to 5 nm.

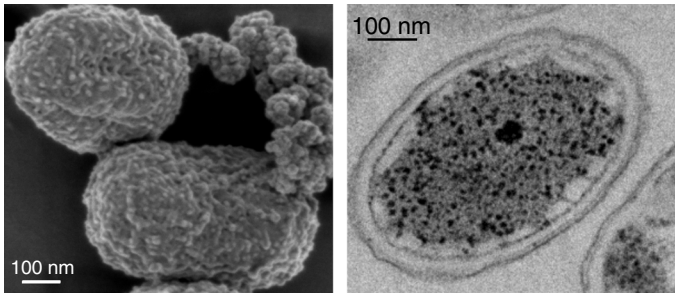

Fig. 3. Scanning electron microscopy and transmission electron microscopy image of strain KB01. Scanning electron photomicrograph (**A**) and transmission electron photomicrograph (**B**) of *C. phaeoferrooxidans* strain KB01 revealing various internal and external cell structures as well as a lack of encrustation (A and B) and a rare association with Fe(III) precipitates (A).

layers rich in anionic functional groups to facilitate attachment to solid substrates (*37*), and these anionic surface functional groups tend to strongly bind Fe(III), effectively neutralizing surface charge (fig. S4). The role of Fe(III) in controlling surface charge on strain KoFox was confirmed by rinsing KoFox cells with reducing agents (sodium dithionite) that liberated Fe(III) and caused a shift in the surface charge to more negative values (fig. S4). These same rinses had little effect on cells of KB01 (fig. S4), confirming the role of surface chemistry and Fe(III) binding in controlling association of cells to Fe(III) (oxyhydr)oxides. The direct role of cell surface charges in dictating mineral association and co-sedimentation is also evident from the strong inverse relationship (fig. S5B) between mineral surface charges and cell-mineral separation.

To assess the biophysical mechanisms that control cell-mineral associations, we determined interfacial properties of the cell and Fe(III) oxyhydroxide surfaces and conducted extended Derjaguin-Landau-Verwey-Overbeek (DVLO) modeling to quantify the forces that develop between these surfaces (Supplementary Materials) (*36*, *38*). DVLO modeling uses measurements of physical surface properties to calculate interfacial forces as a function of distance between surfaces. Our model results revealed that the negative surface charge on strain KB01 led to electrostatic repulsion between its surface and negatively charged Fe(III) (oxyhydr)oxides (Fig. 2C). The more neutral charge on strain KoFox, conversely, led to a weak electrostatic attraction (fig. S5C). Lewis acid-base and Lifshitz–van der Waals forces were much weaker than the electrostatic forces, but we note that the acid-base properties of strain KB01 lead to repulsion of Fe(III) (oxyhydr)oxides, even without electrostatic effects. Surface charge, therefore, controls cell-mineral association, and ultimately like-charged surfaces cause the physical separation of strain KB01 and, by extension, other pelagic photoferrotrophs from their Fe(III) oxyhydroxide by-products. These findings have important implications for BIF deposition and the coupling of carbon and iron cycles in the Archean Eon. We note that while strain KB01 is a derived member of the phylum *Chlorobi*, its cell surface chemistry is typical for Gram-negative bacteria (*30*, *39*), and our results are thus likely extensible to its ancestors and most other Gram-negative bacteria, with the exception of benthic organisms, like strain KoFox, that have unusual modifications to their cell surfaces. Stem group, pelagic photoferrotrophs in Archean oceans, therefore, most likely had cell surface chemistries and interacted with Fe(III) (oxyhydr)oxides much like strain KB01.

Revised Precambrian Fe budgets

Before proceeding to model coupled carbon and iron cycling, we sought to reconcile the possible material fluxes of Fe(II) to the oceans and those needed to sustain BIF deposition (*26*, *40*). These material fluxes serve as boundary conditions for our models and help tether our results to the geologic record. Peak BIF deposition rates imply an Fe burial flux of 45 mol m^{-2} $year^{-1}$ over areas greater than 10^{11} m^2, or ~4.5 Tmol Fe $year^{-1}$ (*5*), and at steady state, Fe(II) must

be actively resupplied to the oceans at this rate through a combination of hydrothermal venting and continental and seafloor weathering. Previous estimates of modern hydrothermal Fe fluxes of ~2 Tmol year^{-1} (Supplementary Materials), on their own, are insufficient to support steady-state BIF deposition (table S3) (*1*, *26*, *40*). These estimates were based on the product of hydrothermal fluid flow and Fe(II) concentrations measured in circulating on- and off-axis fluids (*41*). Global Fe fluxes, however, would have been much different in the Archean Eon because of enhanced hydrothermal activity (*40*, *42*), smaller continents (*43*), reduced seawater sulfate (*42*, *44*), weathering of Earth's crust at low oxygen (*18*, *45*, *46*), and pervasively anoxic oceans.

Hydrothermal fluid fluxes to the oceans have been calculated from a variety of geochemical and physical data resulting in a wide range of estimates for these fluxes in the literature. A recent compilation from a number of sources (*47*), however, provides a synthesis of both on- and off-axis fluid flow as well as a modeled distribution of these values that yields averages (modes) of 5×10^{13} and 1.5×10^{16} kg year^{-1}, respectively (*47*). These values are greater than values considered in previous estimates of modern hydrothermal Fe(II) budgets, implying that modern Fe(II) fluxes to the oceans were underestimated (*41*). Archean hydrothermal fluid flow was, furthermore, likely higher than today due to greater heat loss from the Archean lithosphere (*26*, *48*). Following previous work (*26*), we thus scaled the updated estimates for modern fluid flow by the ratio of past to modern lithospheric heat loss (Supplementary Materials). This yields estimates for hydrothermal fluid flow at 2.5 Ga of $1 \pm 0.6 \times 10^{14}$ and $4 \pm 0.6 \times 10^{16}$ kg year^{-1} for on- and off-axis venting, respectively (table S3). Crucially, these revised estimates for fluid flow increase the possible Fe(II) fluxes to both the modern and Archean oceans.

The concentration of Fe(II) in modern on-axis hydrothermal fluids is ~6 mmol kg^{-1} (*41*), but this depends on the chemistry of seawater that circulates through seafloor basalts. Notably, high concentrations of sulfate (28 mM) in modern seawater lead to production of hydrogen sulfide in anoxic hydrothermal fluids, and this hydrogen sulfide reacts with Fe(II) to form iron-sulfide minerals that limit the concentration of Fe(II) in effluxing fluids (*42*). Sulfate concentrations in Archean seawater were much lower than today due, in part, to the lack of oxidative pyrite weathering on the continents (*44*). Models of hydrothermal fluid chemistry, therefore, predict that Fe(II) concentrations in high-temperature hydrothermal fluids were 10-fold higher when seawater was sulfate free versus the modern 28 mM (*42*), implying that high-temperature vent fluids in the Archean Eon could have had up to 60 mmol kg^{-1} Fe(II). Combining such a high-temperature hydrothermal Fe(II) concentration (*42*) with revised on-axis hydrothermal fluid flows results in Fe(II) fluxes of 8 ± 3 Tmol year^{-1} at 2.5 Ga (table S3), and these are similar to, but smaller than, other recent estimates (*49*). The effect of seawater sulfate concentrations on the Fe(II) concentration in lower-temperature, off-axis hydrothermal fluids appears less pronounced, and so we conservatively consider off-axis hydrothermal Fe(II) concentrations equivalent to today (~0.75 mmol kg^{-1}) (*42*). This results in possible off-axis Fe(II) fluxes of up to 30 ± 5 Tmol year^{-1} (table S3). Combining these new estimates for on- and off-axis Fe(II) fluxes, we redefine upper possible limits on hydrothermal Fe(II) delivery to the oceans at 2.5 Ga as ~40 Tmol year^{-1} (table S3).

In addition to the Fe(II) fluxes from hydrothermal venting, modern continental weathering also contributes Fe to the oceans. We thus assessed the potential delivery flux of continental Fe(II) to Archean oceans, taking into consideration the low oxygen atmosphere (*45*) and smaller continent sizes (*43*), resulting in a total Fe(II) weathering flux of 5 Tmol year^{-1} to the oceans (Supplementary Materials). Summing continental weathering and hydrothermal Fe(II) fluxes yields an upper possible global Fe(II) flux of ~45 Tmol year^{-1} to the oceans 2.5 Ga (table S3). This is more than sufficient to deposit BIF at 4.5 Tmol year^{-1} and is supplied mostly through previously unconsidered off-axis hydrothermal venting. These revised Fe(II) fluxes place upper boundaries on the magnitude of global coupled carbon and iron cycling, which we explore below using biogeochemical box models.

Modeling Archean marine iron and carbon cycles

We assume that biological production in our model is driven by photoferrotrophy, and while oxygenic photosynthesis could have been active from the Mesoarchean (*46*, *50*), its contribution to primary production may have been small before the GOE due to competition with photoferrotrophs (*15*, *51*). Nevertheless, discriminating between modes of photosynthesis would have no real effect on our model outcomes because oxygen produced would react with Fe(II), yielding the same 4:1 stoichiometry between iron oxidation and carbon fixation as in photoferrotrophy. Biomass degradation in our model was first channeled through heterotrophic Fe(III) reduction and then, given the near absence of sulfate in the Archean ocean (*44*), microbial methanogenesis (*22*, *44*). We implicitly assumed that both Fe(III) reduction and methanogenesis are preceded by the breakdown of organic matter through hydrolysis, glycolysis, and fermentation. Rates of organic matter breakdown were parameterized on the basis of observations from modern anoxic marine basins (*52*, *53*). However, we note that, unlike today, the biological pump in the Archean oceans would have operated without ballasting from fecal pellets. Biological production and nutrient cycling in the modern oceans can be divided into three broad oceanographic provinces—open ocean, coastal zone, and upwelling regions (*52*). In detail, the distribution and biological activity of these provinces depend on ocean circulation patterns, continental configurations, and nutrient supply, but in the absence of robust constraints on these parameters for the Archean oceans, we assumed that the relative contributions of similar such provinces to biological production scale with continental area and were otherwise similar to the modern. We thus distributed total biological production across these three provinces according to their relative productivities in the modern ocean (*52*) and scaled continental area from 0 to 100% of the modern (Fig. 4 and Supplementary Materials).

Our results revealed that upwelling provinces support Fe(II) oxidation and Fe(III) oxyhydroxide sedimentation at rates sufficient to deposit even the largest BIFs, such as those of the Hamersley Basin in Western Australia (Fig. 5, Table 1, and Supplementary Materials). Notably, Fe(III) (oxyhydr)oxides, with a relatively high density (3.8 g cm^{-1}) and a tendency to aggregate to larger particle sizes (*54*), had an average settling velocity of 2×10^4 m year^{-1}. This led to their deposition within a maximum of 40 km from their locus of initial precipitation, assuming a 150-m-deep water column and current velocities less than 650 m year^{-1} (fig. S6 and table S4) (*52*, *55*). Furthermore, this localized deposition occurred despite the strong horizontal current velocities that are characteristic of upwelling provinces (*52*, *55*). In stark contrast, the average settling velocity of biomass not associated with Fe(III) (oxyhydr)oxides was 0.35 m year^{-1}, and biomass can thus be transported at distances more than 6000 km—greater than

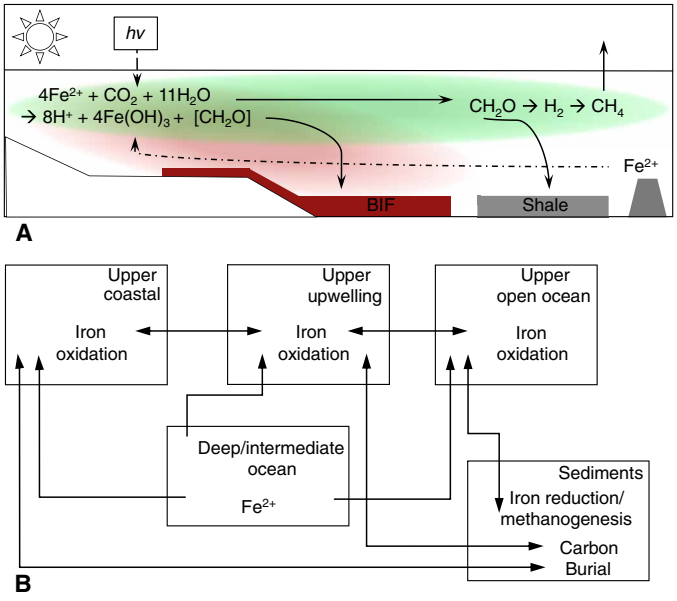

Fig. 4. Model of an Archean coastal upwelling zone. A schematic (**A**) depicting the cycling of iron and carbon in the model and the boxes (**B**) that were used to create the model structure, accompanied by arrows demonstrating the fluxes of various biochemical parameters between the boxes.

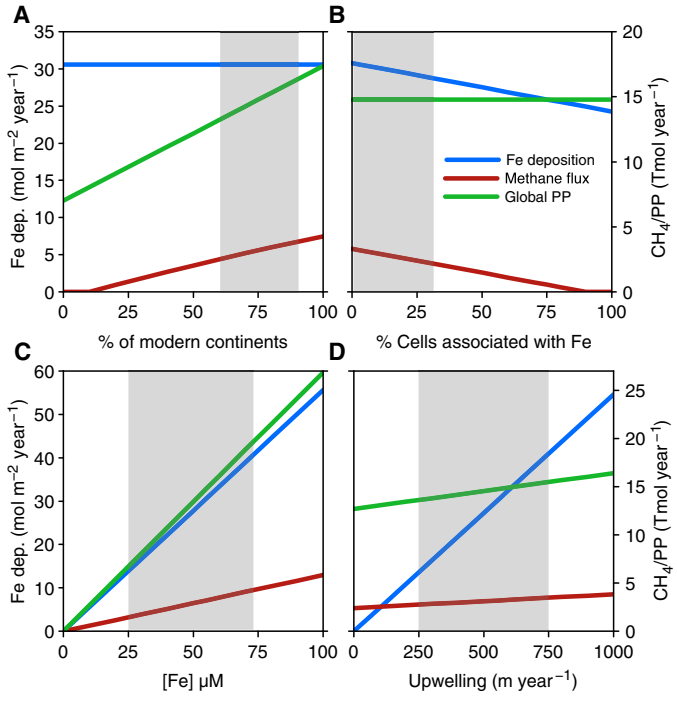

Fig. 5. Iron and carbon box model sensitivity results. (**A**) Model sensitivity results for varying continent size. (**B**) Percentage of cells associated with Fe(III) (oxyhydr) oxides. (**C**) Deep ocean Fe(II). (**D**) Varying upwelling rates in the upwelling provinces. Iron deposition rates in the upwelling provinces are depicted on the *y* axis, while global rates of primary production and methane production are both shown on the *x* axis in Tmol/year.

the width of the modern Pacific Ocean (fig. S6 and table S4). Substantial biomass can thus be exported from productive upwelling areas and broadly distributed between oceanic provinces before its deposition. Notably, the separation of biomass from Fe(III) (oxyhydr) oxides led to little pelagic and sedimentary Fe recycling within the upwelling province itself. The small fraction of biomass deposited in upwelling regions fueled diagenesis, resulting in both Fe(II) recycling to the water column and the authigenesis of reduced Fe phases such as siderite and magnetite. Siderite can be an abundant component in many BIF (*24*, *25*), and an example carbon isotope mass balance suggests that 30% of the siderite in BIFs can be diagenetic, with the balance likely representing a primary precipitate (Supplementary Materials). In our benchmark scenario (Supplementary Materials), where 15% of cells are associated with their Fe(III) by-products, organic carbon deposition rates could have supported the conversion of 10% of the total Fe(III) deposited to diagenetic siderite. When the diagenetic siderite is combined with primary nondiagenetic siderite, as inferred from the isotopic composition of siderite, the total siderite content of BIFs in our benchmark scenario is as high as 30%. This combination of primary and diagenetic siderite and remaining Fe(III) (oxyhydr)oxides yielded an average redox state of Fe in BIF of 2.7 and is very similar to that of many siderite-bearing Neoarchean BIFs (fig. S1 and table S5).

Biomass exported from upwelling provinces augmented the biomass produced in the other provinces and drove extensive pelagic and sedimentary Fe recycling through heterotrophic Fe(III) reduction. As decoupling of biomass from Fe(III) (oxyhydr)oxides in upwelling regions led to excess biomass over Fe(III) in both other provinces, it fueled methanogenesis once Fe(III) had been entirely reduced or was buried as Fe-poor, organic carbon–bearing coastal and deep-sea sediments (Fig. 4). The deposition of biomass in these sediments would have led to organic carbon concentrations of between 0.5 and 5 wt % depending on sedimentation rates of detrital material (Supplementary Materials and fig. S7). At low sedimentation rates characteristic of deep-water environments, organic carbon concentrations are similar to those of the organic carbon–rich shales that deposited throughout the Archean Eon (*45*).

The globally integrated rates of these processes varied depending on continental area, biomass association to Fe(III) (oxyhydr)oxides, Fe(II) concentrations in the deep ocean, and rates of upwelling (Fig. 5). These variables can be constrained to likely ranges based on material fluxes recorded in sedimentary rocks (*1*, *2*, *40*), bounds for global cycling (*1*, *28*, *40*), and tempered analogies to modern systems (*21*, *56*)—model outputs within these ranges are delineated by the shaded area in Fig. 5. Deep ocean Fe(II) concentrations are constrained to <70 μM, similar to earlier estimates of 50 μM based on siderite and calcite solubility (*28*), because higher Fe(II) concentrations led to global Fe(II) oxidation rates that exceed the revised maximum global Fe(II) supplies and recycling combined (table S3). Even at these relatively low Fe(II) concentrations (20 to 70 μM), upwelling provinces could have supported area-specific rates of BIF deposition of up to 54 mol m^{-2} $year^{-1}$ over areas greater than 10^{11} m^2 (Table 1), as needed to deposit the largest of the Archean BIFs (*5*). Notably, with decreased cell-mineral association, increased continent size, increased deep-water Fe(II) concentrations, and increased upwelling rates, Fe(II) consumption could have eventually outpaced even upper limits for Fe(II) supply, and this would have led to depletion of deep ocean Fe(II). Within the most likely parameter space, rates of global primary production through photoferrotrophy would have been less than 1% of modern primary production (Table 1) and, in the absence of oxygen and sulfate, most of this

Table 1. Model results for both the carbon cycle (primary production, carbon burial, carbon remineralization, and methane production) and the iron cycle (iron recycling and iron deposition) at 2.5 Ga. Low, Middle, and High represent the model outputs from the low, middle, and high parts of the ranges depicted by the gray boxes in Fig. 5 and fig. S8. For reference, modern rates of primary production (PP) range from 2760 to 3510 Tmol C year^{-1} (*60*).

	C PP	C burial	C remineralization	C to Fe reduction	C to CH_4 production	Fe recycling	Fe deposition (upwelling province)	Global Fe deposition	Global CH_4
	Tmol C/year	% of PP	% of PP	% of remineralization	% of remineralization	Tmol Fe/year	Tmol Fe/year	Tmol Fe/year	Tmol CH_4/year
2.5 Ga Low	4.5	14.8	85.2	72.6	27.4	11.1	1.0	17.9	0.5
2.5 Ga Middle	14.8	14.7	85.3	49.1	50.9	24.8	9.9	59.1	3.2
2.5 Ga High	22.5	14.6	85.4	41.0	59.0	31.4	17.5	89.9	5.7

biomass would have been remineralized through Fe(III) reduction and methanogenesis in the open ocean, with the remainder buried in sediments (Table 1). Global primary production is limited by P availability over geological time and marine primary production scales with P concentrations in the oceans (*57*). Reconstruction of P concentrations in the Archean oceans implied 0.04 to 0.13 μM (*15*), which is ~1 to 4% of the modern and sufficient to support our estimates for primary production. Notably, up to 45% of all remineralized carbon was channeled through methanogenesis, and the fraction of remineralization through methanogenesis increased with decreased cell-mineral association, increased continent size, increased deep-water Fe(II) concentrations, and increased upwelling rates (Fig. 5 and Table 1). Variations in all of these processes thus likely influenced global rates of iron deposition and methane production and could have contributed to the development of differing BIF facies.

The model prediction that methanogenesis would have played a key role in carbon degradation in Archean ferruginous oceans is also supported by other Earth system models (*49*) and observations from modern ferruginous basins. In Kabuno Bay, East Africa, for example, carbon produced through photoferrotrophy is remineralized through methanogenesis (*21*), leading to an export of ferric iron from the euphotic zone even under extremely quiescent physical conditions. Likewise, despite abundant Fe(III) (oxyhydr)oxides, as much as 50% of the carbon degradation in ferruginous Lake Matano is channeled through methanogenesis, rather than Fe(III) reduction (*56*). Empirical observations thus point generally to carbon and iron cycling under ferruginous conditions that ultimately leads to methane production even in the absence of the large-scale advective processes that operate in the oceans. When integrated into a box model of the Archean marine iron and carbon cycles, our observations of cell-Fe(III) oxyhydroxide separation during photoferrotrophy quantitatively describe an Archean biosphere that: (i) accounts for the Fe(III) deposition rates needed to form BIFs; (ii) explains the fate of biomass and its absence from BIFs; and (iii) provides a strong source of methane to the biosphere.

This model demonstrates that, within the geologically constrained parameter space, global rates of methanogenesis can easily reach 3.2 Tmol year^{-1} (Table 1), and with the near absence of oxygen and sulfate to fuel methane oxidation, most of this methane would be delivered to the atmosphere (*58*). On the basis of new solutions (*49*) to photochemical models (*59*), this biospheric methane flux (3.2 Tmol year^{-1}) would support a 10 ppmv (parts per million by volume) methane atmosphere under our benchmark scenario, with a possible range of between 1 and 20 ppmv across the likely model parameter space (Table 1). While these methane concentrations alone are unlikely to support a warm climate, positive feedbacks with other concurrent modes of photosynthesis, like H_2-based anoxygenic photosynthesis, markedly increase both biospheric methane fluxes to the atmosphere and atmospheric methane concentrations (*49*). Our observations of extant photoferrotrophs, revised global Fe budgets, and models of coupled C and Fe cycling thus support an upside-down Archean biosphere, similar to that originally proposed by Walker (*19*), in which the deposition of BIFs leads to a methane-rich atmosphere. Our results further imply that cell-Fe(III) separation augments marine methane production through the breakdown of photoferrotrophic biomass and mechanistically ties biospheric methane fluxes to the deposition of BIF. The role this plays in atmospheric chemistry and greenhouse warming should be tested through further biogeochemical-photochemical modeling efforts.

METHODS

Photoferrotrophic strains and cyanobacteria were grown in basal media (*21*) and in alternative media (Supplementary Materials and table S1) until late exponential phase. Subsamples of both Fe(II)/Fe(III) and pigments were used to track the growth kinetics and to assess the in vitro cellular association to Fe(III). The surface properties of each strain and their metabolic Fe(III) by-products were assessed by measuring their surface potential using the Particle Metrix ZetaView. The acid-base properties of cell surfaces were determined through titrations. Cell surface contact angles were measured for DVLO modeling in three different liquids—water, glycerol, and diiodomethane (*36*, *38*). Electron microscopies [scanning electron microscopy (SEM) and transmission electron microscopy (TEM)] were used to image cell-mineral interactions (Supplementary Materials). The particle sizes of the Fe(III) (oxyhydr)oxides produced by the photoferrotrophic strains were measured using a Mastersizer 2000 particle size analyzer, and these were then used to model the impact of horizontal ocean

current velocities on the settling time of both Fe(III) particles and cellular biomass (Supplementary Materials, fig. S6, and table S4). The box model of the Archean marine carbon and iron cycles was designed with three boxes (each representing an oceanic province) to capture variability in fluxes through each box (Supplementary Materials, Figs. 4 and 5, fig. S8, and Table 1).

SUPPLEMENTARY MATERIALS

Supplementary material for this article is available at http://advances.sciencemag.org/cgi/content/full/5/11/eaav2869/DC1

Supplementary Materials and Methods

Section S1. Cell surface features and acid-base chemistry

Section S2. Cell-iron surface interaction and extended DVLO modeling

Section S3. Iron concentration and supply

Section S4. Physical separation of ferric iron oxyhydroxides and cellular biomass in an ocean setting

Section S5. Box model of Archean marine carbon and iron cycles

Section S6. Organic carbon burial and diagenesis

Table S1. Range of concentrations in the growth media used throughout experiments.

Table S2. Cell surface characteristics and cell-mineral interaction modeling.

Table S3. Modern and Archean Fe fluxes.

Table S4. Different scenarios of the physical separation model, with each case using a different water velocity.

Table S5. Data compilations for Fig. 1 and fig. S1.

Fig. S1. The redox state of iron in BIF through time where the red bars indicate the siderite-rich BIFs.

Fig. S2. Growth curve for *C. phaeoferrooxidans* strain KB01.

Fig. S3. Additional SEM and TEM images of strains KB01 and KoFox under two conditions.

Fig. S4. Surface charge of strains KB01 and KoFox.

Fig. S5. Additional cell surface characteristics for strain KoFox.

Fig. S6. Modeling the settling velocity of carbon and iron using a range of horizontal current velocities.

Fig. S7. Modeled weight % organic carbon in the coastal and open ocean sediments.

Fig. S8. Iron and carbon box model sensitivity results.

References (*61*–*103*)

View/request a protocol for this paper from *Bio-protocol*.

REFERENCES AND NOTES

1. A. E. Isley, D. H. Abbott, Plume-related mafic volcanism and the deposition of banded iron formation. *J. Geophys. Res. Solid Earth* **104**, 15461–15477 (1999).
2. C. Klein, Some Precambrian banded iron-formations (BIFs) from around the world: Their age, geologic setting, mineralogy, metamorphism, geochemistry, and origins. *Am. Mineral.* **90**, 1473–1499 (2005).
3. P. Cloud, Paleoecological significance of banded iron formation. *Econ. Geol.* **68**, 1135–1143 (1973).
4. R. Garrels, E. Perry, F. Mackenzie, Genesis of Precambrian iron-formations and the development of atmospheric oxygen. *Econ. Geol.* **68**, 1173–1179 (1973).
5. K. O. Konhauser, T. Hamade, R. Raiswell, R. C. Morris, F. G. Ferris, G. Southam, D. E. Canfield, Could bacteria have formed the Precambrian banded iron formations? *Geology* **30**, 1079–1082 (2002).
6. A. Kappler, D. K. Newman, Formation of Fe(III)-minerals by Fe(II)-oxidizing photoautotrophic bacteria. *Geochim. Cosmochim. Acta* **68**, 1217–1226 (2004).
7. B. Rasmussen, B. Krapež, D. B. Meier, Replacement origin for hematite in 2.5 Ga banded iron formation: Evidence for postdepositional oxidation of iron-bearing minerals. *Bulletin* **126**, 438–446 (2014).
8. N. J. Tosca, S. Guggenheim, P. K. Pufahl, An authigenic origin for Precambrian greenalite: Implications for iron formation and the chemistry of ancient seawater. *Bulletin* **128**, 511–530 (2016).
9. F. Widdel, S. Schnell, S. Heising, A. Ehrenreich, B. Assmus, B. Schink, Ferrous iron oxidation by anoxygenic phototrophic bacteria. *Nature* **362**, 834–836 (1993).
10. W. F. Martin, D. A. Bryant, J. T. Beatty, A physiological perspective on the origin and evolution of photosynthesis. *FEMS Microbiol. Rev.*, (2017).
11. W. W. Fischer, J. Hemp, J. E. Johnson, Evolution of oxygenic photosynthesis. *Annu. Rev. Earth Planet. Sci.* **44**, 647–683 (2016).
12. R. E. Blankenship, M. T. Madigan, C. E. Bauer, *Anoxygenic Photosynthetic Bacteria* (Springer Science & Business Media, 2006), vol. 2.
13. D. E. Canfield, M. T. Rosing, C. Bjerrum, Early anaerobic metabolisms. *Philos. Trans. R. Soc. B. Biol. Sci.* **361**, 1819–1834 (2006).
14. P. Kharecha, J. Kasting, J. Siefert, A coupled atmosphere–ecosystem model of the early Archean Earth. *Geobiology* **3**, 53–76 (2005).
15. C. Jones, S. Nomosatryo, S. A. Crowe, C. J. Bjerrum, D. E. Canfield, Iron oxides, divalent cations, silica, and the early earth phosphorus crisis. *Geology* **43**, 135–138 (2015).
16. G. Luo, S. Ono, N. J. Beukes, D. T. Wang, S. Xie, R. E. Summons, Rapid oxygenation of Earth's atmosphere 2.33 billion years ago. *Sci. Adv.* **2**, e1600134 (2016).
17. P. Philippot, J. N. Ávila, B. A. Killingsworth, S. Tessalina, F. Baton, T. Caquineau, E. Muller, E. Pecoits, P. Cartigny, S. V. Lalonde, T. R. Ireland, C. Thomazo, M. J. van Kranendonk, V. Busigny, Globally asynchronous sulphur isotope signals require re-definition of the Great Oxidation Event. *Nat. Commun.* **9**, 2245 (2018).
18. H. D. Holland, The oxygenation of the atmosphere and oceans. *Philos. Trans. R. Soc.* **361**, 903–915 (2006).
19. J. C. Walker, Was the Archaean biosphere upside down? *Nature* **329**, 710–712 (1987).
20. A. Kappler, C. Pasquero, K. O. Konhauser, D. K. Newman, Deposition of banded iron formations by anoxygenic phototrophic Fe(II)-oxidizing bacteria. *Geology* **33**, 865–868 (2005).
21. M. Llirós, T. García-Armisen, F. Darchambeau, C. Morana, X. Triadó-Margarit, Ö. Inceoğlu, C. M. Borrego, S. Bouillon, P. Servais, A. V. Borges, J.-P. Descy, D. E. Canfield, S. A. Crowe, Pelagic photoferrotrophy and iron cycling in a modern ferruginous basin. *Sci. Rep.* **5**, 13003 (2015).
22. K. O. Konhauser, D. K. Newman, A. Kappler, The potential significance of microbial Fe(III) reduction during deposition of Precambrian banded iron formations. *Geobiology* **3**, 167–177 (2005).
23. T. Gauger, J. M. Byrne, K. O. Konhauser, M. Obst, S. Crowe, A. Kappler, Influence of organics and silica on Fe (II) oxidation rates and cell–mineral aggregate formation by the green-sulfur Fe (II)-oxidizing bacterium *Chlorobium ferrooxidans* KoFox–Implications for Fe (II) oxidation in ancient oceans. *Earth Planet. Sci. Lett.* **443**, 81–89 (2016).
24. A. J. Kaufman, J. Hayes, C. Klein, Primary and diagenetic controls of isotopic compositions of iron-formation carbonates. *Geochim. Cosmochim. Acta* **54**, 3461–3473 (1990).
25. C. Klein, N. J. Beukes, Geochemistry and sedimentology of a facies transition from limestone to iron-formation deposition in the early Proterozoic Transvaal Supergroup, South Africa. *Econ. Geol.* **84**, 1733–1774 (1989).
26. R. P. Lowell, S. M. Keller, High-temperature seafloor hydrothermal circulation over geologic time and Archean banded iron formations. *Geophys. Res. Lett.* **30**, (2003).
27. D. E. Canfield, A new model for Proterozoic ocean chemistry. *Nature* **396**, 450 (1998).
28. H. D. Holland, *The Chemical Evolution of the Atmosphere and Oceans* (Princeton Univ. Press, 1984).
29. S. Heising, L. Richter, W. Ludwig, B. Schink, Chlorobium ferrooxidans sp nov., a phototrophic green sulfur bacterium that oxidizes ferrous iron in coculture with a "Geospirillum" sp strain. *Arch. Microbiol.* **172**, 116–124 (1999).
30. J. B. Fein, C. J. Daughney, N. Yee, T. A. Davis, A chemical equilibrium model for metal adsorption onto bacterial surfaces. *Geochim. Cosmochim. Acta* **61**, 3319–3328 (1997).
31. D. A. Sverjensky, N. Sahai, Theoretical prediction of single-site surface-protonation equilibrium constants for oxides and silicates in water. *Geochim. Cosmochim. Acta* **60**, 3773–3797 (1996).
32. K. O. Konhauser, Diversity of bacterial iron mineralization. *Earth Sci. Rev.* **43**, 91–121 (1998).
33. K. O. Konhauser, S. V. Lalonde, L. Amskold, H. D. Holland, Was there really an Archean phosphate crisis? *Science* **315**, 1234 (2007).
34. V. R. Phoenix, D. G. Adams, K. O. Konhauser, Cyanobacterial viability during hydrothermal biomineralisation. *Chem. Geol.* **169**, 329–338 (2000).
35. E. D. Swanner, Physiology, Fe (II) oxidation, and Fe mineral formation by a marine planktonic cyanobacterium grown under ferruginous conditions. *Front. Earth Sci.* **3**, 60 (2015).
36. G. Saini, C. Chan, Near-neutral surface charge and hydrophilicity prevent mineral encrustation of Fe-oxidizing micro-organisms. *Geobiology* **11**, 191–200 (2013).
37. O. Stukalov, A. Korenevsky, T. J. Beveridge, J. R. Dutcher, Use of atomic force microscopy and transmission electron microscopy for correlative studies of bacterial capsules. *Appl. Environ. Microbiol.* **74**, 5457–5465 (2008).
38. C. J. Van Oss, *Interfacial forces in aqueous media* (CRC press, 2006).
39. N. Yee, J. Fein, Cd adsorption onto bacterial surfaces: A universal adsorption edge? *Geochim. Cosmochim. Acta* **65**, 2037–2042 (2001).
40. A. E. Isley, Hydrothermal plumes and the delivery of iron to banded iron formation. *J. Geol.* **103**, 169–185 (1995).
41. S. Poulton, R. Raiswell, The low-temperature geochemical cycle of iron: From continental fluxes to marine sediment deposition. *Am. J. Sci.* **302**, 774–805 (2002).
42. L. R. Kump, W. E. Seyfried, Hydrothermal Fe fluxes during the Precambrian: Effect of low oceanic sulfate concentrations and low hydrostatic pressure on the composition of black smokers. *Earth Planet. Sci. Lett.* **235**, 654–662 (2005).
43. J. Korenaga, *Archean Geodynamics and the Thermal Evolution of Earth* (Geophysical Monograph Series, American Geophysical Union, 2006), pp. 7–32.

44. S. A. Crowe, G. Paris, S. Katsev, C. Jones, S.-T. Kim, A. L. Zerkle, S. Nomosatryo, D. A. Fowle, J. F. Adkins, A. L. Sessions, J. Farquhar, D. E. Canfield, Sulfate was a trace constituent of Archean seawater. *Science* **346**, 735–739 (2014).
45. T. W. Lyons, C. T. Reinhard, N. J. Planavsky, The rise of oxygen in Earth/'s early ocean and atmosphere. *Nature* **506**, 307–315 (2014).
46. S. A. Crowe, L. N. Døssing, N. J. Beukes, M. Bau, S. J. Kruger, R. Frei, D. E. Canfield, Atmospheric oxygenation three billion years ago. *Nature* **501**, 535–538 (2013).
47. I. Halevy, A. Bachan, The geologic history of seawater pH. *Science* **355**, 1069–1071 (2017).
48. N. H. Sleep, K. Zahnle, P. Neuhoff, Initiation of clement surface conditions on the earliest Earth. *Proc. Natl. Acad. Sci. U.S.A.* **98**, 3666–3672 (2001).
49. K. Ozaki, E. Tajika, P. K. Hong, Y. Nakagawa, C. T. Reinhard, Effects of primitive photosynthesis on Earth's early climate system. *Nat. Geosci.* **11**, 55–59 (2017).
50. N. J. Planavsky, D. Asael, A. Hofmann, C. T. Reinhard, S. V. Lalonde, A. Knudsen, X. Wang, F. Ossa Ossa, E. Pecoits, A. J. B. Smith, N. J. Beukes, A. Bekker, T. M. Johnson, K. O. Konhauser, T. W. Lyons, O. J. Rouxel, Evidence for oxygenic photosynthesis half a billion years before the Great Oxidation Event. *Nat. Geosci.* **7**, 283–286 (2014).
51. S. L. Olson, L. R. Kump, J. F. Kasting, Quantifying the areal extent and dissolved oxygen concentrations of Archean oxygen oases. *Chem. Geol.* **362**, 35–43 (2013).
52. J. H. Martin, G. A. Knauer, D. M. Karl, W. W. Broenkow, VERTEX: Carbon cycling in the northeast Pacific. *Deep Sea Res. Part A Oceanogr. Res. Pap.* **34**, 267–285 (1987).
53. A. H. Devol, H. E. Hartnett, Role of the oxygen-deficient zone in transfer of organic carbon to the deep ocean. *Limnol. Oceanogr.* **46**, 1684–1690 (2001).
54. J. F. Banfield, S. A. Welch, H. Zhang, T. T. Ebert, R. L. Penn, Aggregation-based crystal growth and microstructure development in natural iron oxyhydroxide biomineralization products. *Science* **289**, 751–754 (2000).
55. D. Kadko, Upwelling and primary production during the US GEOTRACES East Pacific Zonal Transect. *Global Biogeochem. Cycles* **31**, 218–232 (2017).
56. S. Crowe, S. Katsev, K. Leslie, A. Sturm, C. Magen, S. Nomosatryo, M. A. Pack, J. D. Kessler, W. S. Reeburgh, J. A. Roberts, L. González, G. D. Haffner, A. Mucci, B. Sundby, D. A. Fowle, The methane cycle in ferruginous Lake Matano. *Geobiology* **9**, 61–78 (2011).
57. C. J. Bjerrum, D. E. Canfield, Ocean productivity before about 1.9 Gyr ago limited by phosphorus adsorption onto iron oxides. *Nature* **417**, 159 (2002).
58. D. C. Catling, K. J. Zahnle, C. P. McKay, Biogenic methane, hydrogen escape, and the irreversible oxidation of early Earth. *Science* **293**, 839–843 (2001).
59. A. A. Pavlov, L. L. Brown, J. F. Kasting, UV shielding of NH3 and O2 by organic hazes in the Archean atmosphere. *J. Geophys. Res. Planet* **106**, 23267–23287 (2001).
60. D. Antoine, J. M. André, A. Morel, Oceanic primary production: 2. Estimation at global scale from satellite (coastal zone color scanner) chlorophyll. *Global Biogeochem. Cycles* **10**, 57–69 (1996).
61. F. Hegler, N. R. Posth, J. Jiang, A. Kappler, Physiology of phototrophic iron(II)-oxidizing bacteria: Implications for modern and ancient environments. *FEMS Microbiol. Ecol.* **66**, 250–260 (2008).
62. E. Viollier, P. Inglett, K. Hunter, A. Roychoudhury, P. Van Cappellen, The ferrozine method revisited: Fe (II)/Fe (III) determination in natural waters. *Appl. Geochem.* **15**, 785–790 (2000).
63. N.-U. Frigaard, K. L. Larsen, R. P. Cox, Spectrochromatography of photosynthetic pigments as a fingerprinting technique for microbial phototrophs. *FEMS Microbiol. Ecol.* **20**, 69–77 (1996).
64. A. Korenevsky, T. J. Beveridge, The surface physicochemistry and adhesiveness of Shewanella are affected by their surface polysaccharides. *Microbiology* **153**, 1872–1883 (2007).
65. D. Suter, C. Siffert, B. Sulzberger, W. Stumm, Catalytic dissoluion of iron (III)(hydr) oxides by oxalic acid in the presence of Fe (II). *Naturwissenschaften* **75**, 571–573 (1988).
66. D. R. Lovley, E. J. Phillips, Availability of ferric iron for microbial reduction in bottom sediments of the freshwater tidal Potomac River. *Appl. Environ. Microbiol.* **52**, 751–757 (1986).
67. E. E. Roden, J. M. Zachara, Microbial reduction of crystalline iron (III) oxides: Influence of oxide surface area and potential for cell growth. *Environ. Sci. Technol.* **30**, 1618–1628 (1996).
68. R. E. Martinez, D. S. Smith, K. Pedersen, F. G. Ferris, Surface chemical heterogeneity of bacteriogenic iron oxides from a subterranean environment. *Environ. Sci. Technol.* **37**, 5671–5677 (2003).
69. D. S. Smith, F. G. Ferris, Proton binding by hydrous ferric oxide and aluminum oxide surfaces interpreted using fully optimized continuous p K a spectra. *Environ. Sci. Technol.* **35**, 4637–4642 (2001).
70. R. E. Martinez, D. S. Smith, E. Kulczycki, F. G. Ferris, Determination of intrinsic bacterial surface acidity constants using a Donnan shell model and a continuous pK a distribution method. *J. Colloid Interface Sci.* **253**, 130–139 (2002).
71. J. Cowen, Morphological study of marine bacterial capsules: Implications for marine aggregates. *Mar. Biol.* **114**, 85–95 (1992).
72. C. Van Oss, Hydrophobicity of biosurfaces—Origin, quantitative determination and interaction energies. *Colloids Surf. B Biointerfaces* **5**, 91–110 (1995).
73. D. G. Brown, P. R. Jaffé, Effects of nonionic surfactants on the cell surface hydrophobicity and apparent Hamaker constant of a Sphingomonas sp. *Environ. Sci. Technol.* **40**, 195–201 (2006).
74. W. Norde, J. Lyklema, Protein adsorption and bacterial adhesion to solid surfaces: A colloid-chemical approach. *Colloids Surf.* **38**, 1–13 (1989).
75. J. N. Ryan, P. M. Gschwend, Effects of ionic strength and flow rate on colloid release: Relating kinetics to intersurface potential energy. *J. Colloid Interface Sci.* **164**, 21–34 (1994).
76. S. W. Poulton, D. E. Canfield, Ferruginous conditions: A dominant feature of the ocean through Earth's history. *Elements* **7**, 107–112 (2011).
77. S. M. McLennan, S. Taylor, Continental freeboard, sedimentation rates and growth of continental crust. *Nature* **306**, 169–172 (1983).
78. D. Lowe, Major events in the geological development of the Precambrian Earth, in *The Proterozoic Biosphere: A Multidisciplinary Study* (Cambridge Univ. Press, 1992), pp. 67–75.
79. K. C. Condie, Chemical composition and evolution of the upper continental crust: Contrasting results from surface samples and shales. *Chem. Geol.* **104**, 1–37 (1993).
80. C. Woldringh, J. Binnerts, A. Mans, Variation in Escherichia coli buoyant density measured in Percoll gradients. *J. Bacteriol.* **148**, 58–63 (1981).
81. K. D. Stolzenbach, K. A. Newman, C. S. Wong, Aggregation of fine particles at the sediment-water interface. *J. Geophys. Res. Oceans* **97**, 17889–17898 (1992).
82. W. S. Reeburgh, Oceanic methane biogeochemistry. *Chem. Rev.* **107**, 486–513 (2007).
83. S. Crowe, J. A. Maresca, C. Jones, A. Sturm, C. Henny, D. A. Fowle, R. P. Cox, E. F. Delong, D. E. Canfield, Deep-water anoxygenic photosythesis in a ferruginous chemocline. *Geobiology* **12**, 322–339 (2014).
84. S. A. Crowe, C. Jones, S. Katsev, C. Magen, A. H. O'Neill, A. Sturm, D. E. Canfield, G. D. Haffner, A. Mucci, B. Sundby, D. A. Fowle, Photoferrotrophs thrive in an Archean Ocean analogue. *Proc. Natl. Acad. Sci. U.S.A.* **105**, 15938–15943 (2008).
85. L. Kuntz, T. Laakso, D. Schrag, S. Crowe, Modeling the carbon cycle in Lake Matano. *Geobiology* **13**, 454–461 (2015).
86. P. R. Craddock, N. Dauphas, Iron and carbon isotope evidence for microbial iron respiration throughout the Archean. *Earth Planet. Sci. Lett.* **303**, 121–132 (2011).
87. N. J. Beukes, C. Klein, Geochemistry and sedimentology of a facies transition—from microbanded to granular iron-formation—in the early Proterozoic Transvaal Supergroup, South Africa. *Precambrian Res.* **47**, 99–139 (1990).
88. M. Baur, J. Hayes, S. Studley, M. Walter, Millimeter-scale variations of stable isotope abundances in carbonates from banded iron-formations in the Hamersley Group of Western Australia. *Econ. Geol.* **80**, 270–282 (1985).
89. C. Klein, E. A. Ladeira, Geochemistry and mineralogy of Neoproterozoic banded iron-formations and some selected, siliceous manganese formations from the Urucum District, Mato Grosso do Sul, Brazil. *Econ. Geol.* **99**, 1233–1244 (2004).
90. R. F. Dymek, C. Klein, Chemistry, petrology and origin of banded iron-formation lithologies from the 3800 Ma Isua supracrustal belt, West Greenland. *Precambr. Res.* **39**, 247–302 (1988).
91. C. Klein, N. J. Beukes, Sedimentology and geochemistry of the glaciogenic late Proterozoic Rapitan iron-formation in Canada. *Econ. Geol.* **88**, 542–565 (1993).
92. C. Klein, E. Ladeira, Geochemistry and petrology of some Proterozoic banded iron-formations of the Quadrilátero Ferrífero, Minas Gerais, Brazil. *Econ. Geol.* **95**, 405–427 (2000).
93. H. D. Holland, M. Schidlowski, *Mineral Deposits and the Evolution of the Biosphere* (Springer, 1982).
94. A. R. Cabral, R. A. Creaser, T. Nägler, B. Lehmanna, A. R. Voegelin, B. Belyatsky, J. Pašava, A. A. Seabra Gomes Jr., H. Galbiatti, M. E. Böttcher, P. Escheri, Trace-element and multi-isotope geochemistry of Late-Archean black shales in the Carajás iron-ore district, Brazil. *Chem. Geol.* **362**, 91–104 (2013).
95. Y. Watanabe, H. Naraoka, D. J. Wronkiewicz, K. C. Condie, H. Ohmoto, Carbon, nitrogen, and sulfur geochemistry of Archean and Proterozoic shales from the Kaapvaal Craton, South Africa. *Geochim. Cosmochim. Acta* **61**, 3441–3459 (1997).
96. D. McKirdy, Organic geochemistry in Precambrian research. *Precambrian Res.* **1**, 75–137 (1974).
97. J. J. Middelburg, J. Nieuwenhuize, P. van Breugel, Black carbon in marine sediments. *Mar. Chem.* **65**, 245–252 (1999).
98. A. L. Paropkari, C. P. Babu, A. Mascarenhas, New evidence for enhanced preservation of organic carbon in contact with oxygen minimum zone on the western continental slope of India. *Mar. Geol.* **111**, 7–13 (1993).
99. J. Niggemann, T. G. Ferdelman, B. A. Lomstein, J. Kallmeyer, C. J. Schubert, How depositional conditions control input, composition, and degradation of organic matter in sediments from the Chilean coastal upwelling region. *Geochim. Cosmochim. Acta* **71**, 1513–1527 (2007).

100. C. Klein, E. A. Ladeira, Petrography and geochemistry of the least altered banded iron-formation of the Archean Carajás Formation. *northern Brazil. Econ. Geol.* **97**, 643–651 (2002).
101. C. Klein, Mineralogy and petrology of the metamorphosed Wabush Iron Formation, southwestern Labrador. *J. Petrol.* **7**, 246–305 (1966).
102. N. R. Posth, S. Huelin, K. O. Konhauser, A. Kappler, Size, density and composition of cell–mineral aggregates formed during anoxygenic phototrophic Fe (II) oxidation: Impact on modern and ancient environments. *Geochim. Cosmochim. Acta* **74**, 3476–3493 (2010).
103. D. E. Canfield, Sulfate reduction and oxic respiration in marine sediments: Implications for organic carbon preservation in euxinic environments. *Deep Sea Res. Part A Oceanogr. Res. Pap.* **36**, 121–138 (1989).

Acknowledgments: Anonymous reviewers provided suggestions and criticism. N. Yee, C. Chan, and J. Smit provided insight into cell surface chemistry. Imaging was conducted at the UBC Bioimaging Facility, UBC Pharmaceutical Sciences Imaging Facility, and the SFU 4D LABS Imaging Facility. **Funding:** This work was supported by NSERC Discovery Grant 04867 to S.A.C., NSERC Postgraduate Scholarship–Doctoral Program, and Canada Research Chairs Program. A.K. was supported by the European Research Council under the European Union's Seventh Framework Program (FP/2007–2013)/ERC Grant agreement no. 307320-MICROFOX. **Author contributions:** S.A.C. conceived, designed, and directed the study. S.A.C. and M.L. made observations in Kabuno Bay. K.J.T. performed photoferrotroph cell settling experiments. T.W. performed cyanobacteria settling experiments. K.J.T. and P.A.K. conducted electron microscopy imaging of strain KB01. T.G. and A.K. conducted electron microscopy imaging of strain KoFox. K.J.T., P.A.K., R.L.S., and R.M. characterized cell surface chemistries. K.J.T. conducted DVLO modeling. K.J.T., S.A.C., K.W.B., and C.C.M. constructed the biogeochemical models. K.J.T. and S.A.C. wrote the manuscript with detailed input from P.A.K., K.O.K., C.T.R., and A.K. and contributions from all other authors. **Competing interests:** The authors declare that they have no competing interest. **Data and materials availability:** All data needed to evaluate the conclusions in the paper are present in the paper and/or the Supplementary Materials. Additional data related to this paper may be requested from the authors. Correspondence and requests for materials should be addressed to S.A.C. (sean.crowe@ubc.ca).

Submitted 2 September 2018
Accepted 18 September 2019
Published 27 November 2019
10.1126/sciadv.aav2869

Citation: K. J. Thompson, P. A. Kenward, K. W. Bauer, T. Warchola, T. Gauger, R. Martinez, R. L. Simister, C. C. Michiels, M. Llirós, C. T. Reinhard, A. Kappler, K. O. Konhauser, S. A. Crowe, Photoferrotrophy, deposition of banded iron formations, and methane production in Archean oceans. *Sci. Adv.* **5**, eaav2869 (2019).

Science Advances

Photoferrotrophy, deposition of banded iron formations, and methane production in Archean oceans

Katharine J. Thompson, Paul A. Kenward, Kohen W. Bauer, Tyler Warchola, Tina Gauger, Raul Martinez, Rachel L. Simister, Céline C. Michiels, Marc Llirós, Christopher T. Reinhard, Andreas Kappler, Kurt O. Konhauser and Sean A. Crowe

Sci Adv **5** (11), eaav2869.
DOI: 10.1126/sciadv.aav2869